Multigrid hierarchical simulated annealing method for reconstructing heterogeneous media

Lalit M. Pant,[1] Sushanta K. Mitra,[2] and Marc Secanell[1,*]
[1]*Department of Mechanical Engineering, University of Alberta, Edmonton, Canada T6G 2G8*
[2]*Department of Mechanical Engineering, York University, Toronto, Canada M3J 1P3*
(Received 3 September 2015; revised manuscript received 7 November 2015; published 4 December 2015)

A reconstruction methodology based on different-phase-neighbor (DPN) pixel swapping and multigrid hierarchical annealing is presented. The method performs reconstructions by starting at a coarse image and successively refining it. The DPN information is used at each refinement stage to freeze interior pixels of preformed structures. This preserves the large-scale structures in refined images and also reduces the number of pixels to be swapped, thereby resulting in a decrease in the necessary computational time to reach a solution. Compared to conventional single-grid simulated annealing, this method was found to reduce the required computation time to achieve a reconstruction by around a factor of 70–90, with the potential of even higher speedups for larger reconstructions. The method is able to perform medium sized (up to 300^3 voxels) three-dimensional reconstructions with multiple correlation functions in 36–47 h.

DOI: 10.1103/PhysRevE.92.063303 PACS number(s): 05.10.−a, 05.40.−a

I. INTRODUCTION

A detailed knowledge of the structure of porous media is paramount in many engineering and geological applications, such as electrochemical systems, CO_2 sequestration, food processing, and textiles. Several parameters, such as porosity, pore size, pore connectivity, surface area, and percolating volume dictate its physical properties. It is therefore critical to develop methodologies to analyze, reconstruct, and design porous structures. Porous media can be characterized by several stochastic correlation functions, such as n-point correlation functions, lineal path function, and chord length function [1]. The complete characterization of the microstructure is known to be dependent upon an infinite set of such n-point correlation functions [1]. In reality, however, only a selected few of these correlation functions can be computed. Reconstructing the microstructure from a limited number of statistical descriptors is an inverse problem, which has gained significant interest in recent years [2].

Several stochastic methods have been proposed in the literature to reconstruct porous media [3–19,19–29]. Initials attempts used a Gaussian random field truncated by linear and nonlinear filters [3–6]. The filters correlated the truncated field to the two-point correlation functions. This method, although reasonably accurate and fast, has its limitations, as one can only use two-point correlation functions. Other two-point statistics-based methods include the gradient-based method [30] and phase recovery method [31]. These methods use fast Fourier transforms (FFT) for estimating two-point statistics, which are then used for reconstruction purposes. Due to the restriction of using only two-point statistics, these methods suffer from the same issues as the Gaussian field methods. To overcome these issues, the simulated annealing (SA) method was proposed [10,14,15]. The simulated annealing method is based on a Monte Carlo process, where an initial random field is slowly changed (annealed) to a final structure with correlation functions as close as possible to the target [15,28]. The SA method can include as many correlation functions as practically possible [15,28], and therefore can result in a reconstruction that better represents the original structure. The method of simulated annealing has been extensively used for reconstructing porous media structures and suspensions [12–16,19,20,24,26,28]. Apart from correlation functions, the raster path method [27] and multiple point statistics have also been used with SA to improve long-range connectivity of the reconstructed phases [18,19,32].

Even with the advantages of including several correlation functions and enhanced accuracy, the conventional simulated annealing method still suffers from two major issues:

(1) *Reconstruction speed:* The conventional simulated annealing method with random pixel swapping is extremely slow, especially at the final stages of reconstruction [20,24,28]. Further, the time to compute the updated correlation functions after swap is directly dependent on the image size, i.e., the larger the image size, the more time it takes to compute the function. This causes the reconstruction method to become impractical for large image sizes, as the method can take several weeks to obtain a single structure. It is therefore imperative to improve the reconstruction speed of the method.

(2) *Reduced long-range connectivity:* Due to random swapping, final reconstructed images with SA have many isolated pixels left. These stray pixels contribute to dead volume (nonconnectivity) and reduce the long-range connectivity of the reconstructed image compared to the reference image. The inability to reproduce long-range connectivity is inherent to the SA technique and is exacerbated for large image sizes. Since the SA method works by pixel swapping (i.e., a minor structure perturbation at a time), the probability that a large-scale feature, such as connected cluster can be reproduced by multiple repetitive minor perturbations is low. Each pixel swap is a local scale interaction, which cumulatively is unlikely to generate a large-scale global feature.

To overcome the disadvantages associated with random pixel swapping, biased pixel swapping methods have been recently proposed [20,24,28]. Tang *et al.* [24] and Pant *et al.* [28] showed that a different-phase-neighbor (DPN) based method reduces the reconstruction steps significantly and also removes the number of unphysical isolated pixels, thereby improving the overall accuracy of the reconstruction.

*secanell@ualberta.ca; www.esdlab.mece.ualberta.ca

The DPN-based method gives priority to pixels which are surrounded by more pixels of different phases. The DPN method, however, has not been studied extensively, and most studies have dealt with small three-dimensional (3D) images (e.g., upto 128^3 voxels). Even though the DPN method reduces the required number of swaps, each swap takes a longer amount of time due to the extra computations. For large image sizes, therefore, even the DPN method in its current state is not practical.

Multigrid hierarchical simulated annealing (HSA) methods have been presented in the literature to overcome the disadvantages associated with large image sizes [29,33–35]. In the HSA method, the large-scale refined structures are obtained by successively refining and annealing coarser structures. Reconstruction at each scale is treated as an independent simulated annealing problem. Initial attempts by Campaigne *et al.* [33] and Alexander *et al.* [34] used a simple hierarchical annealing where the reconstruction is started at a coarse scale. Then, after achieving convergence at the coarse scale, the image is refined and further annealed. This process is repeated until the desired reconstruction size has been obtained. Even though this method showed some improvements in reconstruction speed, it also has several issues. Since each step is treated as an independent SA problem, the structure generated at the coarse scale can be melted during reconstruction at refined scales, unless the annealing temperature is precisely controlled. Furthermore, the swapping procedure can still permutate among all the pixels at the refined scale, thereby keeping the computational cost high. The frozen state methods presented by Campaigne and Fieguth [35] and Chen *et al.* [29] resolve these issues. The frozen state methods generate the large-scale structures at the coarse scales and keep them frozen at refined scales (i.e., the frozen pixels are not allowed to be swapped at refined scales). Only local fine-resolution details are added with scale refinement (image size increase), which significantly reduces the number of pixels available for swapping. These method has shown significant speed advantages compared to conventional methods [35].

Even with all the advantages of the frozen-state HSA method, only a few studies in the literature have explored it. Campaigne and Fieguth [35] used neighborhood matching instead of correlation function optimization with the gray-scale HSA method. It is therefore unclear how much of the reported time advantage is due to the HSA method and how much is due to introducing neighborhood matching. To the best of authors' knowledge, only Chen *et al.* [29] have used it for 3D image reconstruction with correlation functions but have not presented any comparison with other methods. Furthermore, it has not been used in conjunction with DPN-based swapping. The DPN-based method may be able to further improve the accuracy of the HSA method. Apart from the speed and accuracy advantages of the DPN method, it provides an easy way to freeze pixels during refinement. While Campaigne and Fieguth [35] and Chen *et al.* [29] introduce an extra gray phase for freezing, DPN-based methods can simply assign a zero priority to the frozen pixels. This greatly reduces the implementation complexity and provides both the benefits of DPN and HSA.

This article presents a DPN-assisted frozen-state hierarchical annealing method. This method uses DPN information for freezing pixels during refinement, thereby eliminating the need for introducing gray-scale pixels. This is a continuation of earlier work by Pant *et al.* [28], combining the speed and accuracy of DPN method with a multigrid methodology. These improvements were necessary for medium-size 3D reconstructions to be effectively performed. A comparison to other methods in the literature is also provided and the differences between methods are discussed. Section II presents an overview of the reconstruction methodology used with an explanation of the multigrid methodology. Section III discusses the results and findings of the work and compares our results to other methods in the literature. Finally, Sec. IV summarizes the findings of the article.

II. RECONSTRUCTION METHODOLOGY

Consider a heterogeneous media with N phases. A statistical descriptor for some phase $j(j \in [1,N])$ is expressed as $f_0^{(j)}(r)$ for the reference image. The same statistical descriptor for the reconstructed image is expressed as $f_{r,t}^{(j)}(r)$ during a particular step t of the reconstruction procedure. Consider that M such descriptors are being used to characterize the media. The discrepancy of the structure at step t compared to the target (reference) structure is expressed as the L_2 norm-based error in the statistical descriptors. The total discrepancy in the heterogeneous media is expressed as:

$$E_t = \sum_{i=1}^{M} \sum_{j=1}^{N} \sum_{r=0}^{r_{\max}} \alpha_{ij} \left[f_{i,0}^{(j)}(r) - f_{i,r,t}^{(j)}(r) \right]^2, \tag{1}$$

where r is the length at which the statistical descriptor is evaluated; i represents the type of correlation function, e.g., two-point correlation function, lineal path function or chord length function; and α_{ij} is the weight assigned to the energy of phase j using the correlation function i. The aim of the reconstruction procedure is to evolve the structure in such a way that the energy goes to zero (or it is at least minimized to a practically negligible value). Several different types of statistical descriptors (correlation functions) can be used for the reconstruction. In this study, two-point correlation function $[S_2(r)]$, lineal path function $[L(r)]$, chord length function $[C(r)]$, and two-point cluster function $[C_2(r)]$ are used for analysis and/or reconstruction. Details of these correlation functions, including the evaluation methods have been discussed in detail by Yeong and Torquato [15] and Pant *et al.* [28].

A. Simulated annealing

Simulated annealing is a Monte Carlo process–based energy minimization algorithm, which resembles the method used to anneal molten metal [10,15]. At each step of the simulated annealing, two pixels from different phases are interchanged (this keeps the volume fractions constant). This interchange will modify the correlation functions and, as a result, will also modify the system energy E_t. If the energy after interchange is represented as E_{t+1}, then the energy change will be calculated as $\Delta E_t = E_{t+1} - E_t$. Depending on the sign of the energy change, the interchange will either take the structure closer to the reference structure (negative energy change)

or away from it (positive energy change). The interchange has traditionally been accepted using the probability-based selection rule by Metropolis *et al.* [36]. In recent work, Pant *et al.* [28] have shown that a threshold-based selection rule results in marginally faster reconstructions without any compromise in accuracy. Using the threshold-based rule, the pixel swap at any step t is accepted with the following probability [28,37]:

$$p(\Delta E_t) = \begin{cases} 1, & \Delta E_t \leqslant E_{\text{th}}, \\ 0, & \text{otherwise}, \end{cases} \tag{2}$$

where E_{th} is known as the threshold energy for acceptance ($E_{\text{th}} \geqslant 0$). The reconstruction procedure starts with a high threshold energy, which is equivalent to high annealing temperature, and allows all possible moves that can result in a reconstruction. The threshold energy is then slowly reduced mimicking the cooling in annealing, so in later stages only energy decreasing moves are accepted. Like a thermal annealing process, the threshold energy is slowly reduced in small steps. The methodology for determining the cooling schedule and the initial threshold energy have been discussed in previous work [28].

B. Pixel swapping method

Several methods are used in the literature for the pixel interchange at each reconstruction step, such as random [15], interfacial [16,38] or DPN-based swapping [20,24,28]. Comparison studies carried out by Tang *et al.* [24] and Pant *et al.* [28] showed that, among all these methods, the DPN-based method can achieve the most accurate reconstructions in the least number of reconstruction steps. A detailed description of the methodology has been given by Tang *et al.* [24] and Pant *et al.* [28].

The DPN-based method favors the pixels with higher number of different phase neighbors. The neighbors of a pixel are defined as the pixels that are a pixel distance away either along axes or along diagonals, as shown in Fig. 1. The different phase neighbor count is equal to the number of neighbors that do not belong to the phase of the pixel of interest. The maximum possible number of DPNs are 8 and 26 in 2D and 3D geometries, respectively.

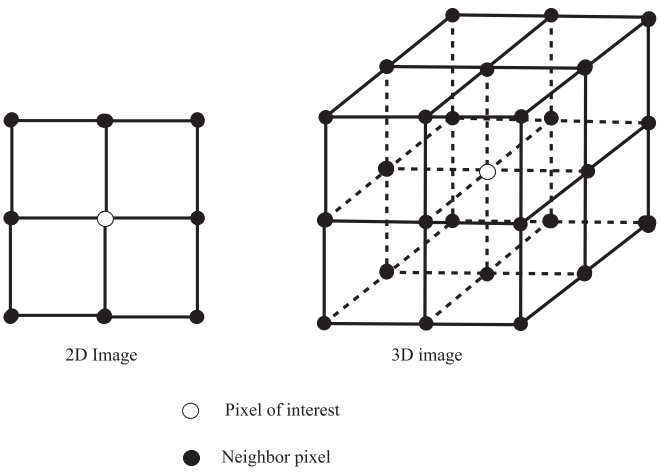

FIG. 1. Neighborhood of a pixel in a 2D and 3D image.

The first step of the DPN method is grouping pixels in each phase with the same number of DPNs. Define $n(S_i)$ as the number of pixels with i DPNs. Define also the probability of selecting a pixel from this group as $p(S_i)$. The maximum DPN in the system is then defined as M, where $M = \max(i) : n(S_i) \neq 0$. The probability of selecting a pixel from any set is given as follows:

$$p(S_i) = \omega n(S_i)\sqrt{i} \qquad i = 0,1 \ldots M, \tag{3}$$

where ω is a normalization factor. Since the probabilities for all sets should add up to 1, ω is found using:

$$\sum_{i=0}^{M} p(S_i) = \sum_{i=0}^{M} \omega n(S_i)\sqrt{i} = 1. \tag{4}$$

With this probability distribution, a DPN set is selected and a random pixel is picked from the selected DPN set. The same procedure is used to select a pixel from another phase. The two selected pixels are then swapped. The expression for the probability of selecting a pixel differs from Tang *et al.* [24] and Pant *et al.* [28] because this expression was found to better reconstruct the porous media structures in a computationally efficient manner.

C. Multigrid hierarchical annealing

To solve the problem of slow convergence in large-scale reconstruction problems, a DPN-based multigrid hierarchical annealing method is proposed. The multigrid method is initiated by reconstructing a small-scale coarse image, which is then continuously refined until the desired size has been achieved. At each scale, the reconstruction is performed as an independent simulated annealing problem. Two critical parts of the multigrid method are the reference image synthesis and the reconstructed image refinement.

To perform a reconstruction at coarser scales (small size), a reference image is required at the corresponding scale. Figure 2 shows the schematic of the process for synthesizing coarse reference images from the original high-resolution image. Let Ω^s represent a binary image at refinement scale s, where increasing s represents a coarser image. The binary image is represented as a collection of pixel values Ω^s_{ij}. The pixel values at a coarser scale s are obtained by averaging the values of its parent pixels at finer scale $s-1$, where the average is represented as $\overline{\Omega}^{s-1}_{ij}$

$$\Omega^s_{ij} = \begin{cases} 0 & \text{if } \overline{\Omega}^{s-1}_{ij} < 126.5, \\ 255 & \text{if } \overline{\Omega}^{s-1}_{ij} > 126.5, \\ 0 \text{ or } 255 & \text{otherwise (i.e., } \overline{\Omega}^{s-1}_{ij} = 126.5). \end{cases} \tag{5}$$

For the third case, the pixel values are randomly assigned in such a way that the volume fraction of each phase is conserved; however, due to the digitized nature of the image, the volume fractions may not stay exactly the same at each scale. This method can be thought of as a two-step process, which involves image coarsening followed by image thresholding. It is evident that the uncertain pixels in the reference images will always end up at the interfaces of coarser images.

The second part of the multigrid process is the refinement of images during reconstruction. The reconstruction starts at

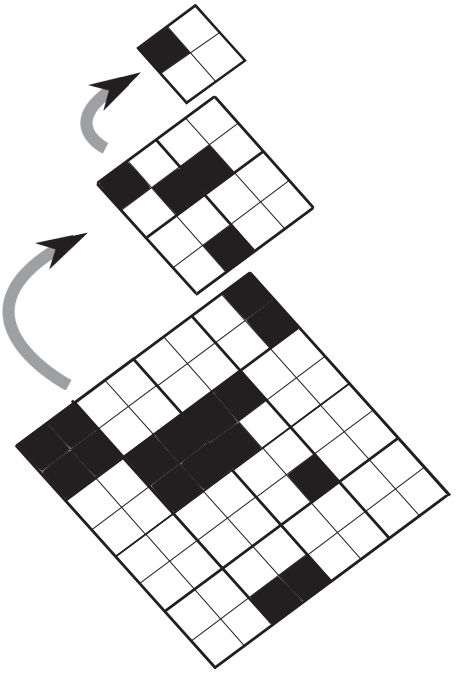

FIG. 2. Schematic depicting the reference image synthesis for smaller scales (black and white colors show two different phases).

the coarsest scale, where the reconstruction is performed using SA for the required size. Once a final solution is obtained, each pixel is broken into four new pixels (children pixels), which are then assigned a phase and a frozen status. This process is repeated until a reconstruction at desired size has been obtained. To avoid deterioration of the coarse scale structures, all the internal pixels are frozen in the refinement, and the interfacial pixels are nonfrozen. In this work, the interfacial pixels can be handled using one of two separate methods: (1) all the children of interfacial pixels at the coarse scale are allowed to be swapped at the next refined scale or (2) only the interfacial pixels in the refined structure are allowed to be swapped. When an interfacial pixel at the coarse scale is refined, not all of its children will necessarily be at the interface in the refined image. Since the second method does not allow the noninterfacial children to be swapped, it will reduce the number of pixels to be swapped.

Figure 3 shows the schematic of image synthesis and pixel freezing for method 1. The frozen status of a pixel in the refined image is decided based on its parent's DPN value. Children of all the pixels with nonzero DPN (interfacial pixels) at the coarse scale are not frozen, while the rest of the pixels are frozen. If the parent of a pixel (Ω_{ij}^{s}) at a refined scale s is Ω_{ij}^{s+1} at a coarse scale $s+1$, then the refined image will be synthesized as:

$$\begin{aligned} \mathrm{Color}\left(\Omega_{ij}^{s}\right) &= \mathrm{Color}\left(\Omega_{ij}^{s+1}\right), \\ \mathrm{Status}\left(\Omega_{ij}^{s}\right) &= \begin{cases} \text{Frozen} & \text{if } n_{\mathrm{DPN},ij}^{s+1} = 0 \\ \text{Not frozen} & \text{otherwise,} \end{cases} \end{aligned} \tag{6}$$

where $n_{\mathrm{DPN},ij}^{s+1}$ is the number of different phase neighbors for the parent pixel at coarse scale.

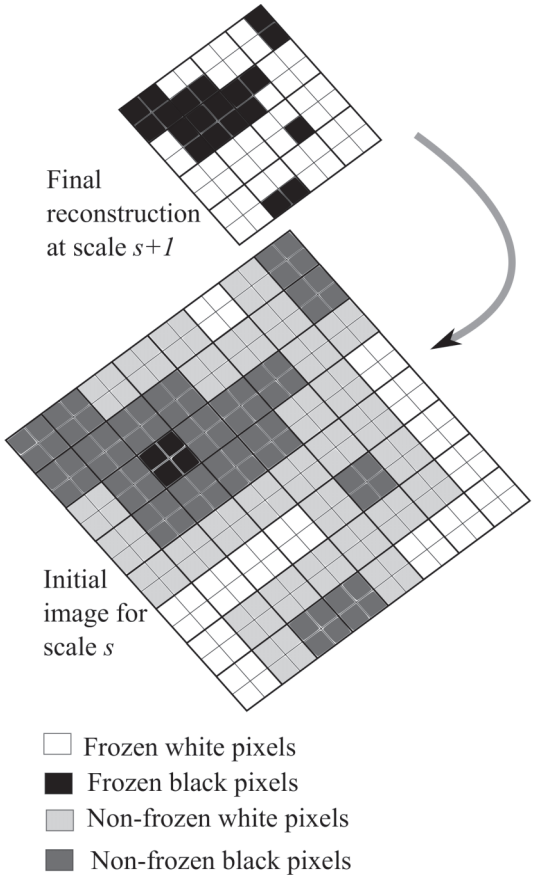

FIG. 3. Schematic depicting the reconstructed image refinement and pixel freezing using method 1. DPN values are calculated using periodic boundaries on the images (black and white show two different phases. Gray is only used for depiction of frozen state and does not represent a new phase).

For method 2, the frozen status is defined based on the DPN of the refined image itself, and the image is synthesized as:

$$\begin{aligned} \mathrm{Color}\left(\Omega_{ij}^{s}\right) &= \mathrm{Color}\left(\Omega_{ij}^{s+1}\right), \\ \mathrm{Status}\left(\Omega_{ij}^{s}\right) &= \begin{cases} \text{Frozen} & \text{if } n_{\mathrm{DPN},ij}^{s} = 0 \\ \text{Not frozen} & \text{otherwise.} \end{cases} \end{aligned} \tag{7}$$

Not only is the freezing status determined using the DPN information of the image, it also is enforced using the DPN methodology. While assembling the pixels in different DPN sets, all the pixels with a frozen status are not included in the sets. This ensures that the frozen pixels are not included in the swapping process and are therefore not moved. In summary, the DPN-assisted multigrid hierarchical annealing method uses DPN values to freeze the interior pixels of clusters at refined scales. This ensures that the structure does not erode at refined scales, irrespective of the threshold energy or temperature schedule. The swapping of interfacial pixels allows the small-scale features to develop at refined scales while keeping the majority of the structure intact. This method also reduces the number of visited pixels at refined stages without needing to introduce gray-scale values.

D. Computational implementation

An in-house code has been developed in C++ using object-oriented programming for the multigrid hierarchical annealing process. The overall algorithm of the multigrid method is given by Algorithm 1. It is essentially an extended and improved version of the earlier 2D algorithm by Pant *et al.* [28]. Some of the critical features of the reconstruction program are as follows:

(a) The correlation functions for each line of the image are stored, and after each swap, only the lines belonging to the swapped pixels are updated. This saves an enormous amount of time, as the whole image does not need to be analyzed.

(b) Computation of DPN sets is an extremely time-consuming task, especially for large images. This program saves the DPN information of the entire image and implements efficient updating algorithms to only update the DPN information in the neighborhood of the swapped pixels. The DPN sets are only computed at the beginning of the reconstruction at each image refinement and are only updated after each swap. This results in time saving of several order of magnitude for large images.

Algorithm 1 Algorithm for DPN assisted multigrid hierarchical simulated annealing

```
Read original reference image Ω^0_ref;
Define number of multigrid stages as n;
for i = 1 to n-1 do
    Generate coarse image Ω^i_ref from Ω^{i-1}_ref ;
end for
for i = n-1 to 0 do
    procedure OBTAIN THE STARTING IMAGE FOR STAGE i
        if i == (n-1) then                    ▷ First (coarsest) stage
            Generate random pixel distribution;
            Set all pixels as not frozen;
        else                                  ▷ Some refinement stage
            Get reconstructed image at scale i + 1;
            Get DPN information at scale i + 1;
            Generate pixel color values using Eq. (6) or (7);
            Generate pixel status using Eq. (6) or (7);
        end if
    end procedure
    procedure OBTAIN RECONSTRUCTION FOR STAGE i
        Read starting image (Ω^i_rec);
        while E > E_tol and Iter_failed < Iter_failed,max do
            Swap two pixels among not frozen set;
            Compute update correlation functions;
            Compute new energy and ΔE;
            Compute applicable threshold energy E_th;
            if ΔE ≤ E_th then
                Accept pixel swap;
                Update image information;
                Reset Iter_failed;
            else
                Reset image information;
                Increment Iter_failed;
            end if
            Increment total iterations;
        end while
        Save the final image Ω^i_rec;
    end procedure
end for
```

(c) The program uses openMP interface for parallel computing. Even though the overall Monte Carlo process cannot be run in parallel due to its sequential nature (each step depends on the previous step), the computations related to each swap can be performed in parallel.

III. RESULTS

The aim of this article is to introduce a DPN-based multigrid hierarchical simulated annealing method which can accurately reconstruct large images with minimal computational cost. The multigrid method was compared against conventional single grid simulated annealing and the effect of coarsening stages was studied. Since reconstructing a large 3D image (e.g., a 600^3 voxel image) with a single grid method takes an impractical amount of time, initial comparison studies were done using a 2D image of size 600^2 pixels. The 2D image reconstructions are also easier for visualization and qualitative assessment. The two freezing methods were also compared. Finally, the best methods were used to reconstruct 3D images of a fuel cell catalyst layer (CL) and a ceramic with a size of 300^3 voxels. Multiple correlation functions were used to reconstruct the 3D structures and an optimum combination was obtained for the best overall optimization. All the simulations were performed using a PC with Intel(R) Xeon(R) E5-2690 CPU with clock speed of 3.00 GHz. The PC runs on an openSUSEx86_64 operating system.

A. Multigrid reconstruction of 2D images

A scanning electron micropscope (SEM) image of an inkjet printed fuel cell CL [39] was taken as the reference image of 2D reconstructions [see Fig. 4(a)]. The image was resized to a size of 600^2 pixels and binarized using the Otsu algorithm [40] in IMAGEJ software [41]. The final reference image is shown in Fig. 4(b). As discussed in Sec. I, one of the major factors in deciding the reconstruction time is the time required to compute correlation functions. A study on the computation time for different correlation functions was performed using different image sizes. The maximum span of the correlation functions was kept fixed. Figure 5 shows the increase in computation time as the image size increases. For a given span size, the computation time increases linearly with image size

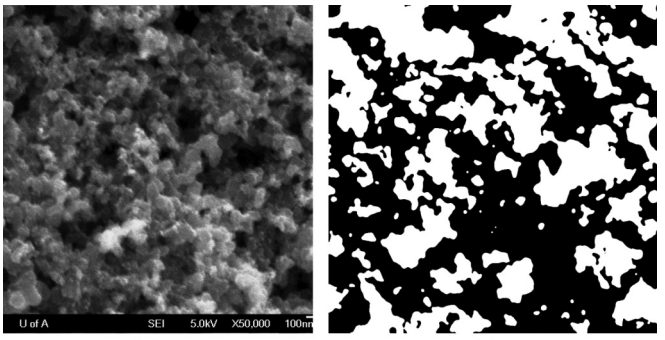

(a) (b)

FIG. 4. Images of a fuel cell catalyst layer. (a) Original SEM image. (b) Binarized image used as the reference image for 2D reconstruction (black shows the solid phase, and white shows the void phase).

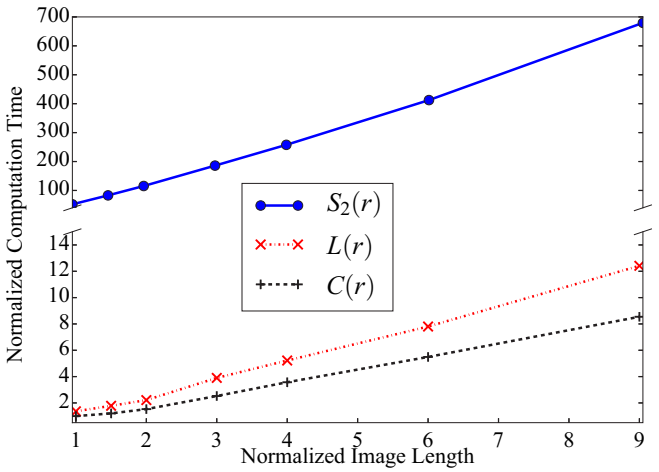

FIG. 5. (Color online) Effect of image size on computation time for different correlation functions. The time is normalized by computation time of chord length function for a size of 100 pixels.

for all correlation functions. The increment factor was found to be higher for two-point correlation functions compared to lineal path and chord length functions. For an n times increase in image size, the computation time increased by $1.5n$, $1.02n$, and $0.96n$ times for $S_2(r)$ (two-point correlation function), $L(r)$ (lineal path function), and $C(r)$ (chord length function), respectively. It was also found that the absolute time taken by $S_2(r)$ is higher than the time taken by $L(r)$ and $C(r)$ by a factor of the span (in this study 50). During reconstruction, the computational time increment factor is expected to be slightly higher, as the spans of the correlation functions also increase with image sizes.

It is evident that image size plays a critical role in reconstruction time. In the multigrid method, the reconstruction sizes can be decreased by introducing additional coarse grid levels. The effect of grid levels was studied by performing reconstructions using different grid levels. The binary SEM image shown in Fig. 4(b) was used as a reference image. A void phase two-point correlation function $[S_2^{(v)}(r)]$ is used for reconstruction. The general simulated annealing parameters are shown in Table I. For an explanation of the parameters

TABLE I. General simulated annealing parameters used for multigrid reconstruction.

Parameter	Value
Reconstructed image size	600×600 pixels
Number of multigrid levels	Varies (1–4)
Maximum allowed failed iterations	10^5
Target energy	10^{-6}
Markov chain size	5000
Energy threshold update factor (λ)	0.95
Initial energy factor (p_0)	0.5
Initial iterations (t_0)	5000
Correlation functions used	$S_2^{(v)}(r)$
Cutoff energy for switching to DPN	5×10^{-3}
Initial energy factor after starting DPN	0.25
Number of processors	2

TABLE II. Comparison of average reconstruction times for different multigrid reconstructions (final image size 600×600). The margins of error are based on 10 trials and represent a 95% confidence interval

Type of reconstruction	Reconstruction time (min)	Average advantage ($\bar{t}_{\text{single}}/\bar{t}$)
Single level	448.34 ± 1.8	1
Two levels (Freeze$_1$)	45.46 ± 0.56	9.86
Three levels (Freeze$_1$)	38.09 ± 1.55	11.77
Four levels (Freeze$_1$)	35.38 ± 0.43	12.67
Two levels (Freeze$_2$)	42.38 ± 0.39	10.57
Three levels (Freeze$_2$)	30.53 ± 0.35	14.66
Four levels (Freeze$_2$)	28.69 ± 0.24	**15.62**

not defined in this article, please refer to the previous work by Pant *et al.* [28]. Table II shows the average reconstruction time for different multigrid levels. The margins of error are reported for 10 samples with a 95% confidence interval and are calculated using Microsoft EXCEL. The levels refer to the number of grid levels used for reconstruction, e.g., a single grid means reconstruction on original size, two levels means reconstruction at a coarse scale (300×300) followed by reconstruction at the final scale (600×600), and so on. Freeze$_1$ refers to instances where freezing was done using method 1, i.e, Eq. (6), whereas Freeze$_2$ refers to instances where freezing was done using method 2, i.e., Eq. (7). The results clearly show that increasing grid levels reduces the reconstruction time; however, the incremental reduction in time is reduced with each additional grid level. It is therefore expected that coarsening below a certain size by adding more grid levels will not result in additional time savings. By introducing four grid levels, the reconstruction time reduced by a factor of 15. The reduction factor will be dependent on the final reconstruction size, i.e., time advantages will be more substantial for larger images than for smaller ones. The reconstruction time for very large images (e.g., above 2000^2 pixels) may, however, still be high enough to make reconstruction impractical. The proposed method therefore is suitable only for medium image sizes.

There are two primary reasons for the observed reduction in the reconstruction time with more grid levels: (a) The reduction in image size for coarser grid levels and (b) the smaller number of pixels to permutate at higher sizes. As all the interior pixels are frozen at coarse scales, very few of the pixels need to be visited by the swapper at refined scales. This reduces the total number of required swaps and hence the reconstruction time. Figure 6 shows the fraction of nonfrozen pixels at each grid scale (ratio of image size at current scale to the image size at finest scale). The fraction of permuting pixels at the finest scale is around 0.1–0.2, thereby reducing the number of swaps required at the finest scale by a significant amount compared to a conventional method, where all the pixels are permuting at the finest scale. As expected, Freeze$_2$ freezes more pixels at each stage compared to Freeze$_1$, which results in Freeze$_2$ providing more time advantage compared to Freeze$_1$.

The energy evolution for the Freeze$_2$-based method was also studied for different grid levels. Figure 7 shows multiple energy evolutions during reconstruction for a different number of multigrid levels. The starting energy is lower when more

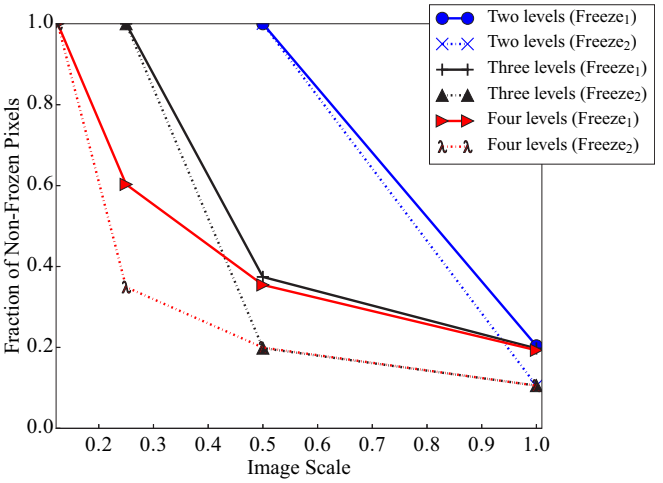

FIG. 6. (Color online) Fraction of nonfrozen (permutating) pixels at each refinement level for multigrid methods. Values show average over 10 trials. Margins of error are less than 1% and therefore not visible in the plot.

coarse levels are introduced, as it reduces the starting image size. Since the starting energy is lower, fewer iterations will be required to converge to a given final tolerance. The number of iterations at the finest level (towards the end of the reconstruction) become smaller with increasing grid levels due to the pixel freezing. Since image size is one of the main contributing factors towards computational time, fewer iterations at higher sizes will result in significant time reduction.

Figure 8 shows the evolution of the reconstructed image through all the grid levels (indicated by s). The overall structure does not change significantly after the first grid level. After each refinement, most of the changes occur at the interfaces, where more refinements to the structure are added. Due to the use of DPN-based pixel swapping, almost no isolated pixels remain in the final reconstruction.

The overall effect of image size on total reconstruction time was also studied. Table III shows the average computational

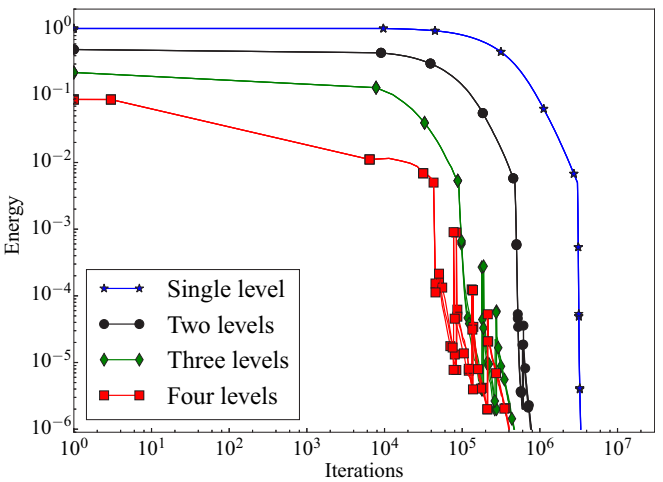

FIG. 7. (Color online) Change in energy with reconstruction progress for different grid-based methods.

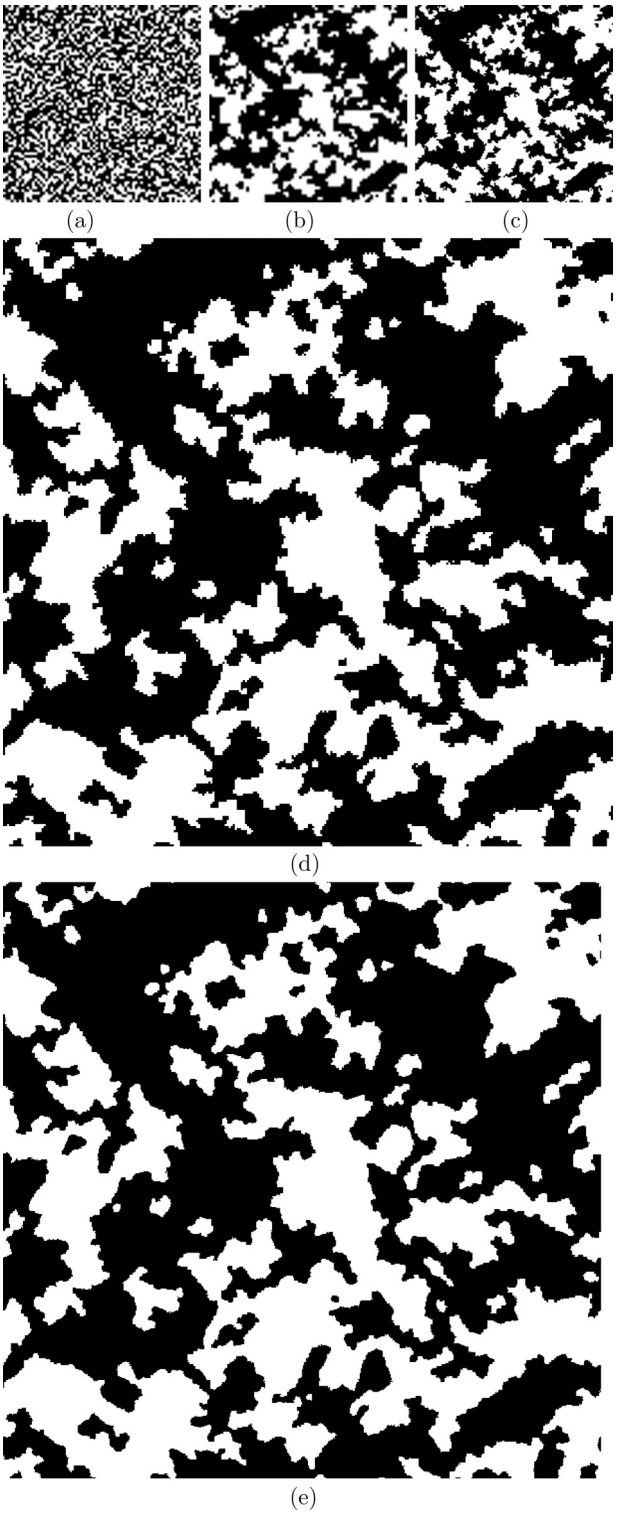

FIG. 8. Reconstructed images at different scales using the multigrid method (black shows the solid phase, and white shows the void phase). Images are to scale. (a) Initial starting image for $s = 3$. (b) Reconstructed image for $s = 3$. (c) Reconstructed image for $s = 2$. (d) Reconstructed image for $s = 1$. (e) Final reconstructed image ($s = 0$).

time for reconstructing 2D CL images of different sizes using $S_2^{(v)}(r)$. The Freeze$_2$ method with four grid levels was used for all image sizes. The overall time for reconstruction increases

TABLE III. Reconstruction time for different final reconstructed image sizes. All reconstructions are performed using Freeze_1 with four grid levels. The margins of error are based on 10 trials and represent a 95% confidence interval.

Image size	Image size increment factor ($L/80$)	Reconstruction time (min)	Average time increment ($\bar{t}/\bar{t}_{80}$)
80×80	1	1.45 ± 0.25	1
160×160	2	3.36 ± 0.25	2.31
240×240	3	4.85 ± 0.20	3.34
320×320	4	7.19 ± 0.20	4.95
400×400	5	13.02 ± 0.41	8.79
600×600	7.5	28.69 ± 0.24	19.78

nonlinearly with increase in image size. The increase in time can be divided into two parts: (1) Time increase due to additional cost of computing $S_2^{(v)}(r)$, which increases by a factor of approximately 1.5 with image size, and (2) time increase due to more pixel swaps (i.e., more iterations) at larger image sizes. It can be observed that the time increment due to increase in swaps is higher than the time increment due to increase in correlation function computing time. Due to the nonlinear increase in reconstruction time, reconstructing very large images (2000^2 pixels or bigger) may become impractical.

All the reconstructions so far have been performed by minimizing the energy based on only the void phase two-point correlation function. The primary advantage of the simulated annealing method is the ability to include more correlation functions to better characterize the porous structure. Therefore, more reconstructions were performed using different correlation functions and combinations. In the earlier study by Pant *et al.* [28], a combination of void phase two-point correlation function [$S_2^{(v)}(r)$], void phase lineal path function [$L^{(v)}(r)$], and solid phase lineal path function [$L^{(s)}(r)$] was found to result in the best overall optimization. Similar results are observed in the current study. Table IV shows the discrepancy in each correlation function for the best [$S_2^{(v)}(r)$, $L^{(v)}(r)$, and $L^{(s)}(r)$] and worst case [$S_2^{(v)}(r)$ only] reconstruction scenarios. A visual comparison between the correlation functions of reference and reconstructed images can be found in the Supplemental Material [42, Section 1.1]. It can be observed that not only the error in $L^{(v)}(r)$ and $L^{(s)}(r)$ has reduced as expected, the error in $C^{(v)}(r)$ and $C^{(s)}(r)$ has also reduced. Qualitatively, the reconstructed images look similar to Fig. 8(e) and therefore are not shown. The two-point cluster functions could not be optimized using any of the other functions, as it essentially represents three-dimensional connectivity of porous media and is not applicable to the 2D cases. Three-dimensional reference and reconstructed images are required to completely characterize and compare the cluster functions in a porous medium. The addition of several correlation functions to the objective energy function results in an increase in computational requirements. Whereas the four grid level reconstruction using only $S_2^{(v)}(r)$ on two processors took 28.68 ± 0.24 minutes, the average time using $S_2^{(v)}(r)$, $L^{(v)}(r)$, and $L^{(s)}(r)$ on three processors was around 288.6 ± 39.1 min. This time, however, is still much lower than the time taken by conventional single grid method using only $S_2^{(v)}(r)$, as shown in Table II.

B. Multigrid reconstruction of 3D images

Once the two-dimensional reconstructions were completed and an optimal set of parameters was obtained, three-dimensional reconstruction of porous media was studied. Since the primary aim of the reconstruction process is to provide a physical domain for studying physical processes in the porous media, 3D reconstructions are critical to assess the performance of any reconstruction methodology. For this study, 3D reconstructions of two porous media, (1) a fuel cell CL and (2) a ceramic, were performed. For the CL, the SEM image shown in Fig. 4(b) is used for 3D reconstructions as well. Figure 9 shows the binary x-ray microtomography image of the ceramic used as a reference image for the reconstruction. These two porous media were chosen in order to test the reconstruction method on both high- and low-porosity media. Also, these two media have different porous structures and therefore different energy landscapes during reconstruction. Since the information in the third direction is not available, the reference correlation functions in the z direction are obtained by averaging the x and y direction correlation functions of the 2D reference image. Three grid levels are used for reconstructing a CL of size 300^3 voxels and a ceramic of size 300^3 voxels. Freeze_2 is used for pixel freezing and three processor cores are used for all the 3D reconstructions. The rest of the parameters are the same as shown in Table I.

First, 3D reconstructions were created by using only two-point correlation function. Figure 10(a) shows the reconstructed 3D image of CL and Fig. 10(b) shows a reconstructed 3D image of the ceramic. The interior cross sections of the 3D structures are also shown to analyze the pore connectivity and internal features. Qualitatively, the reconstructed images show similar features to their reference images with good connectivity of the pore and solid phases. Five reconstructions

TABLE IV. Comparison of discrepancy in different correlation functions for 2D reconstructions using different correlation function combinations. Both sets used four grid levels. The margins of error are based on 10 trials and represent a 95% confidence interval.

	Average $L2$ norms of error for the function						
Functions used	$S_2^{(v)}(r)$	$C_2^{(v)}(r)$	$C_2^{(s)}(r)$	$L^{(s)}(z)$	$L^{(v)}(z)$	$C^{(s)}(z)$	$C^{(v)}(z)$
$S_2^{(v)}(r)$	$(9.99 \pm 0.00) \times 10^{-7}$	$(4.61 \pm 2.06) \times 10^{-1}$	(3.26 ± 2.88)	$(3.71 \pm 0.79) \times 10^{-2}$	$(1.20 \pm 0.33) \times 10^{-2}$	$(3.72 \pm 0.22) \times 10^{-3}$	$(3.94 \pm 0.20) \times 10^{-3}$
$S_2^{(v)}(r)$, $L^{(v)}(r)$ $L^{(s)}(r)$	$(1.83 \pm 0.11) \times 10^{-7}$	$(6.64 \pm 3.64) \times 10^{-1}$	(4.30 ± 4.08)	$(2.31 \pm 1.04) \times 10^{-6}$	$(5.14 \pm 1.07) \times 10^{-7}$	$(7.28 \pm 0.32) \times 10^{-4}$	$(9.85 \pm 0.42) \times 10^{-4}$

FIG. 9. Binarized SEM image of a ceramic used as reference image for 3D reconstruction (black shows the solid phase, and white shows the void phase).

of each media were performed using $S_2^{(v)}(r)$. The average time taken for the reconstructions to converge to an energy of 10^{-6} was 22.67 ± 0.11 h for CL and 27.39 ± 0.03 h for ceramic. The reason for difference in reconstruction times is likely due to the difference between the correlation functions of the CL and ceramic (see the Supplemental Material [42, Section 2]). This may result in a more complex energy landscape for ceramic and therefore a higher computational time. Even though these reconstruction times may appear large in absolute terms, it must be noted that single grid instances of these reconstructions using conventional random swapping did not converge even after one and a half months. For example, the energy for the ceramic went from 0.2 to approximately 3×10^{-4} in 35 days. Given that the energy reduction is slower at later stages, it can be expected that a final convergence to

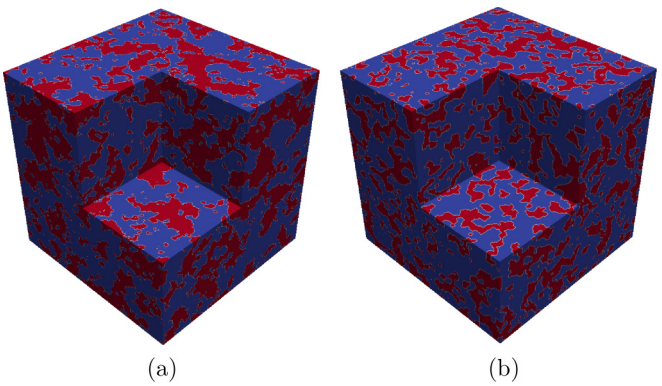

FIG. 10. (Color online) 3D reconstructions using only $S_2^{(v)}(r)$. Blue shows the solid phase and red shows the void phase. (a) Catalyst layer; (b) ceramic.

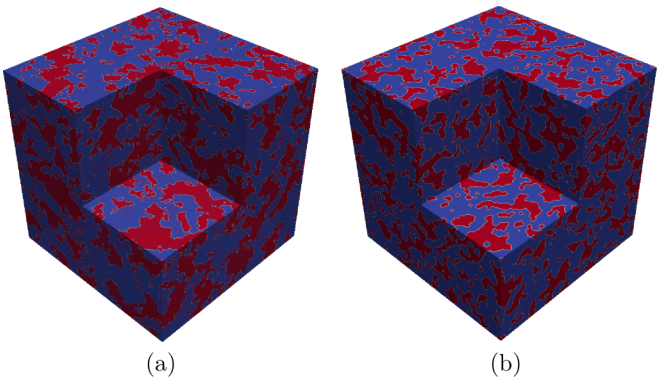

FIG. 11. (Color online) 3D reconstructions using $S_2^{(v)}(r)$, $L^{(v)}(r)$, and $L^{(s)}(r)$. Blue shows the solid phase and red shows the void phase. (a) Catalyst layer and (b) ceramic.

10^{-6} would have taken at least 30–40 additional days. Based on this, it can be concluded that the DPN and multigrid method provided at least around a 70- to 90-times speedup.

After obtaining 3D reconstructions based on only two-point correlation functions, reconstructions were performed using several correlation function combinations. Similarly to the 2D images, the combination of $S_2^{(v)}(r)$, $L^{(v)}(r)$, and $L^{(s)}(r)$ was found to result in the best overall optimization of the structure. Figure 11(a) shows the reconstructed 3D image of the CL, and Fig. 11(b) shows a reconstructed 3D image of the ceramic using this combination. Qualitatively, the images are similar to the reference images and also to the two-point correlation-function-based reconstructions shown in Fig. 10. Looking at the internal cross sections of the reconstructed images, the phase connectivity seems to have improved compared to only $S_2^{(v)}(r)$-based reconstructions. For quantitative comparison, the discrepancy in all the correlation functions is computed and compared between the different reconstructions. Table V shows the average discrepancy in all correlation functions for the different reconstructions. A visual comparison between the correlation functions of reference and reconstructed images can be found in the Supplemental Material [42, Section 1.2]. It can be observed that the addition of $L^{(v)}(r)$ and $L^{(s)}(r)$ not only decreases the discrepancy of $L^{(v)}(r)$ and $L^{(s)}(r)$ as expected but also decreases the discrepancy of $C^{(v)}(r)$ and $C^{(s)}(r)$. This improvement in statistical accuracy could, however, differ for other porous media and for the physical properties of the porous media. Since a 2D reference image is used, the cluster functions are still not properly characterized, resulting in high discrepancy of $C_2^{(v)}(r)$ and $C_2^{(s)}(r)$.

Similarly to the 2D images, the improvement in the reconstruction comes at the cost of reconstruction time. While the $S_2^{(v)}(r)$-based reconstruction times for CL and ceramic were 22.67 ± 0.11 h and 27.39 ± 0.03 h, respectively, $S_2^{(v)}(r)$-, $L^{(v)}(r)$-, and $L^{(s)}(r)$-based reconstruction times were 36.85 ± 0.41 h for CL and 47.19 ± 0.41 h for ceramic. As with the $S_2^{(v)}(r)$-based reconstructions, ceramic reconstructions take longer to perform than CL. The addition of correlation functions increases the reconstruction time. There are two primary reasons for the time increase. First, addition of extra correlation functions requires extra computations after each

TABLE V. Comparison of discrepancy in different correlation functions for 3D reconstructions using different correlation function combinations. The margins of error are based on five trials and represent a 95% confidence interval.

		Average L2 norms of error for the function						
Porous media	Functions used	$S_2^{(v)}(r)$	$C_2^{(v)}(r)$	$C_2^{(s)}(r)$	$L^{(s)}(z)$	$L^{(v)}(z)$	$C^{(s)}(z)$	$C^{(v)}(z)$
CL	$S_2^{(v)}(r)$	$(1.00 \pm 0.00) \times 10^{-6}$	$(9.24 \pm 0.03) \times 10^{-2}$	$(6.76 \pm 0.06) \times 10^{-2}$	$2.96 \pm 0.25) \times 10^{-2}$	$(2.89 \pm 0.22) \times 10^{-3}$	$(5.52 \pm 0.06) \times 10^{-3}$	$6.61 \pm 0.04) \times 10^{-3}$
	$S_2^{(v)}(r)$, $L^{(v)}(r), L^{(s)}(r)$	$(5.71 \pm 0.17) \times 10^{-7}$	$(9.18 \pm 0.01) \times 10^{-2}$	$(6.77 \pm 0.02) \times 10^{-2}$	$(1.00 \pm 0.00) \times 10^{-6}$	$(5.36 \pm 0.11) \times 10^{-7}$	$(2.61 \pm 0.07) \times 10^{-3}$	$(2.86 \pm 0.07) \times 10^{-3}$
Ceramic	$S_2^{(v)}(r)$	$(1.00 \pm 0.00) \times 10^{-6}$	$(3.11 \pm 0.00) \times 10^{-2}$	$(1.37 \pm 0.00) \times 10^{-2}$	$(2.67 \pm 0.51) \times 10^{-2}$	$(9.80 \pm 1.01) \times 10^{-3}$	$(9.46 \pm 0.07) \times 10^{-3}$	$(1.19 \pm 0.00) \times 10^{-2}$
	$S_2^{(v)}(r)$, $L^{(v)}(r), L^{(s)}(r)$	$(6.57 \pm 0.11) \times 10^{-7}$	$(3.08 \pm 0.01) \times 10^{-2}$	$(1.37 \pm 0.00) \times 10^{-2}$	$(1.00 \pm 0.00) \times 10^{-6}$	$(8.68 \pm 0.44) \times 10^{-7}$	$(6.49 \pm 0.16) \times 10^{-3}$	$(7.52 \pm 0.12) \times 10^{-3}$

swap, thereby increasing the total reconstruction time. Second, the energy landscape with multiple correlation function may be more complex than with a single correlation function, thereby requiring more time to exit local minima.

It is evident from these studies that the use of the proposed multigrid method results in a significant amount of time savings compared to the conventional single-grid method. Table VI shows a comparison of reconstruction times between the current work and the limited information available in literature (unfortunately, very few articles in the reconstruction literature report the computing specifications and times). It can be seen that the proposed method outperforms all single-grid methods [17,21,25,28]. Among the single-grid methods, the one by Capek *et al.* [21] shows the most promising results due to fine-tuned simulated annealing parameters and an adaptive temperature schedule; however, the proposed method outperforms it even when using all three correlation functions for reconstruction.

The multigrid methods by Alexander *et al.* [34] and Campaigne and Fieguth [35] seem to largely outperform the proposed method in terms of reconstruction time. These method, however, use either neighborhood matching [35] (instead of correlation function optimization) or a higher energy tolerance [34]. The final energy in Refs. [34,35] is three orders of magnitude higher, i.e., $\geqslant 10^{-3}$, than our current method. A higher tolerance in our method results in a dramatic decrease in computational time. For example, the average reconstruction time [$S_2^{(v)}(r)$ based] for reconstructing a 2D

TABLE VI. Comparison of simulated annealing-based reconstruction times in the literature to the proposed method. Acronyms used are as follows, SG, single grid; MG, multigrid; PA, probability-based selection; TA, threshold-based selection; RND, random swapping; INT, interfacial swapping; DPN, DPN-based swapping; GSM, gray-scale methods (multigrid) using extra phase for freezing; and E_f, final energy of the reconstructed structure. Neighborhood refers to the cases where local neighborhood matching is carried out instead of correlation function optimization.

Ref.	System specs.	Correlation functions	Size	Reconstruction time (h)	Remarks
Current work	Intel E5-2690 3.00 GHz	$S_2^{(v)}(r)$	600×600	0.5	Unified DPN ($a = 0$, $b = 0.5$), MG, TA, $E_f = 10^{-6}$
		$S_2^{(v)}(r) + L^{(v)}(r) + L^{(s)}(r)$		5	
		$S_2^{(v)}(r)$	300^3	22–28	
		$S_2^{(v)}(r) + L^{(v)}(r) + L^{(s)}(r)$		36–47	
		$S_2^{(v)}(r) + C^{(s)}(r)$	500×500	220	RND, SG, PA, $E_f = 10^{-4}$
[17]	IBM RS/6000	$C^{(v)}(r) + C^{(s)}(r)$	500×500	55	
[21]	SGI Altix 350, 1.5 Ghz	$S_2^{(v)}(r) + L^{(v)}(r)$ or $S_2^{(v)}(r) + L^{(s)}(r)$	320^3	160–400	INT, SG, PA, $E_f \sim \mathcal{O}(10^{-7})$, Adaptive temperature
[25]	Chebyshev supercomputer	$S_2^{(v)}(r)$	200×200	48–72	RND, SG, PA, $E_f = 10^{-7}$
[28]	Intel E5-2690 3.00 GHz	$S_2^{(v)}(r)$	200×200	1.5	DPN, SG, TA, $E_f = 10^{-6}$
		$S_2^{(v)}(r) + L^{(v)}(r) + L^{(s)}(r)$	200×200	15	
		$S_2^{(v)}(r) + C^{(v)}(r)$	512×512	0.25	RND,MG, PA, $E_f = 0.483$
[34]	N/A	Neighborhood	8192×8192	96	RND, MG, PA, $E_f \sim \mathcal{O}(10^{-3})$[a]
[35]	N/A	Neighborhood	512×512	0.04	RND, GSM, PA, $E_f \sim \mathcal{O}(10^{-3})$[a]
			8192×8192	2–14	

[a] E_f is not known from the reference article. Approximate value is estimated from the available comparison of reference and reconstructed correlation functions.

image of size 600×600 with a final energy of 1×10^{-3} was 0.1 ± 0.006 h, which is less than half of the time reported by Alexander *et al.* [34] for a similarly sized 2D image. When compared to Campaigne and Fieguth [35], it must be noted that the total time saving is due to the gray-scale method as well as neighborhood matching. Comparing the reported time (0.1 ± 0.006 h) to the one for a similarly sized image using the method by Campaigne and Fieguth [35], it can be seen that the combination of gray-scale method and neighborhood matching results in a speed advantage of around 2 times. Based on this result, it appears that the major time advantage of Campaigne and Fieguth's [35] method over the proposed method may be due to the use of neighborhood matching and not to the use of the gray-scale-based pixel freezing.

In summary, the proposed method based on multigrid hierarchical SA with DPN-based pixel selection outperforms all conventional single grid methods and the multigrid method by Alexander *et al.* [34]. The gray-scale method by Campaigne and Fieguth [35] is faster than the proposed method due to the use of neighborhood matching; however, the correlation function of the reconstruction does not match the reference image statistical correlation functions very well [the $L2$ norm is approximately $\sim\mathcal{O}(10^{-3})$]. Even though the proposed method is able to perform medium size (200–600 pixel length) reconstructions in practical amounts of time, it may still not be suited for very large scale image reconstructions (600^3 and above).

IV. CONCLUSIONS

A multigrid hierarchical simulated annealing with a DPN-based pixel selection reconstruction method has been presented. The method performs reconstructions at small length scales and successively refines them. DPN information is used to freeze pixels at higher length scales in order to preserve the large-scale structure and reduce reconstruction time. The method uses efficient DPN storage and updating methods to reduce computational costs, especially for large image sizes. Several 2D reconstructions were used to compare the method to the conventional single grid methodology. The multigrid method was found to result in a speedup factor of around 70–90 compared to single grid methods, which can be even more for larger image sizes. Use of the proposed method in reconstructing 3D images of size 300^3 with multiple correlation functions showed that it is capable of reconstructing porous structures with high accuracy in practical amounts of time. A comparison with literature results shows that the method introduced largely outperforms all the other simulated annealing-based methods, and the multigrid method by Alexander *et al.* [34]. The gray-scale multigrid method by Campaigne and Fieguth [35] appears to be superior to the proposed method; however, the gray-scale method is more difficult to implement and the performance benefits may be primarily due to neighborhood matching.

ACKNOWLEDGMENTS

The authors thank Carbon Management Canada (CMC), Natural Sciences and Engineering Research Council of Canada (NSERC), Canada Foundation for Innovation (CFI), University of Alberta doctoral recruitment scholarship, and Alberta Innovates - Technology Futures Graduate Student Scholarship for financial assistance. The authors also thank Kailyn Domican at ESDL, University of Alberta, for providing the SEM images of catalyst layers. Finally, the authors thank Kirill Gerke at CSIRO, Land and Water Division, Australia, for providing the x-ray microtomography image of the ceramic material.

[1] S. Torquato, *Random Heterogeneous Materials:Microstructure and Macroscopic Properties* (Springer, New York, 2000).
[2] Y. Jiao, F. H. Stillinger, and S. Torquato, Phys. Rev. E **76**, 031110 (2007).
[3] J. Cahn, J. Chem. Phys. **42**, 93 (1965).
[4] M. Joshi, A class of stochastic models for porous materials, Ph.D. thesis, University of Kansas, 1974.
[5] J. Quiblier, J. Colloid Interface Sci. **98**, 84 (1984).
[6] P. Adler, C. Jacquin, and J. Quiblier, Int. J. Multiphase Flow **16**, 691 (1990).
[7] J. Poutet, D. Manzoni, F. Hage-Chehade, C. Jacquin, M. Bouteca, J.-F. Thovert, and P. Adler, Int. J. Rock Mech. Mining Sci. Geomech. **33**, 409 (1996).
[8] M. Giona and A. Adrover, AIChE J. **42**, 1407 (1996).
[9] N. F. Berk, Phys. Rev. Lett. **58**, 2718 (1987).
[10] A. Ouenes, S. Bhagavan, P. Bunge, and B. Travis, in *Proceedings of Society of Petroleum Engineers* (Society of Petroleum Engineers Inc., New Orleans, LA, 1994), pp. 547–560.
[11] R. Hazlett, Math. Geol. **29**, 801 (1997).
[12] A. Roberts and M. Teubner, Phys. Rev. E **51**, 4141 (1995).
[13] A. P. Roberts and M. A. Knackstedt, Phys. Rev. E **54**, 2313 (1996).
[14] M. Rintoul and S. Torquato, J. Colloid Interface Sci. **186**, 467 (1997).
[15] C. L. Y. Yeong and S. Torquato, Phys. Rev. E **57**, 495 (1998).
[16] M. G. Rozman and M. Utz, Phys. Rev. E **63**, 066701 (2001).
[17] M. Talukdar, O. Torsaeter, and M. Ioannidis, J. Colloid Interface Sci. **248**, 419 (2002).
[18] H. Okabe and M. J. Blunt, Phys. Rev. E **70**, 066135 (2004).
[19] H. Okabe and M. J. Blunt, J. Pet. Sci. Eng. **46**, 121 (2005).
[20] X. Zhao, J. Yao, and Y. Yi, Transp. Porous Media **69**, 1 (2007).
[21] P. Capek, V. Hejtmanek, L. Brabec, A. Zikanova, and M. Kocirik, Transp. Porous Media **76**, 179 (2009).
[22] P. Capek, V. Hejtmanek, J. Kolafa, and L. Brabec, Transp. Porous Media **88**, 87 (2011).
[23] Y. Jiao, F. Stillinger, and S. Torquato, Proc. Natl. Acad. Sci. USA **106**, 17634 (2009).
[24] T. Tang, Q. Teng, X. He, and D. Luo, J. Microsc. **234**, 262 (2009).
[25] K. Gerke, M. Karsanina, and E. Skvortsova, Eurasian Soil Sci. **45**, 861 (2012).
[26] A. Hajizadeh and Z. Farhadpour, Transp. Porous Media **94**, 859 (2012).

[27] P. Tahmasebi and M. Sahimi, Phys. Rev. Lett. **110**, 078002 (2013).
[28] L. M. Pant, S. K. Mitra, and M. Secanell, Phys. Rev. E **90**, 023306 (2014).
[29] D. D. Chen, Q. Teng, X. He, Z. Xu, and Z. Li, Phys. Rev. E **89**, 013305 (2014).
[30] D. Fullwood, S. Kalidindi, S. Niezgoda, A. Fast, and N. Hampson, Mater. Sci. Eng. A **494**, 68 (2008).
[31] D. Fullwood, S. Niezgoda, and S. Kalidindi, Acta Mater. **56**, 942 (2008).
[32] A. Hajizadeh, A. Safekordi, and F. Farhadpour, Adv. Water Resour. **34**, 1256 (2011).
[33] W. Campaigne, P. Fieguth, and S. Alexander, *3rd International Conference on Image Analysis and Recognition*, Lecture Notes in Computer Science (including subseries Lecture Notes in Artificial Intelligence and Lecture Notes in Bioinformatics) Vol. 4141 (Springer, Berlin, 2006), p. 41.
[34] S. Alexander, P. Fieguth, M. Ioannidis, and E. Vrscay, Math. Geosci. **41**, 357 (2009).
[35] W. Campaigne and P. Fieguth, IEEE Transact. Image Process. **22**, 1486 (2013).
[36] N. Metropolis, A. Rosenbluth, M. Rosenbluth, A. Teller, and E. Teller, J. Chem. Phys. **21**, 1087 (1953).
[37] G. Dueck, J. Comput. Phys. **90**, 161 (1990).
[38] Y. Jiao, F. H. Stillinger, and S. Torquato, Phys. Rev. E **77**, 031135 (2008).
[39] S. Shukla, K. Domican, K. Karan, S. Bhattacharjee, and M. Secanell, Electrochim. Acta **156**, 289 (2014).
[40] N. Otsu, IEEE Transact. Syst. Man Cybern. **9**, 62 (1979).
[41] W. Rasband, IMAGEJ (1997), US National Institutes of Health, Bethesda, Maryland, USA.
[42] See Supplemental Material at http://link.aps.org/supplemental/10.1103/PhysRevE.92.063303 for information on correlation functions of the two porous media.